Optimal location of the two-element rectangular rosette to evaluate the stress intensity factor K I

F. Mejni, T. Kanit, J-M. Nianga, A. Imad

Version of Record: https://www.sciencedirect.com/science/article/pii/S0167844220302603
Manuscript_dec45212d02a1f12ecc44602b32d3c44

Optimal location of the two-element rectangular rosette to evaluate the stress intensity factor K_I

F. Mejni[1,2], T. Kanit[*,2], J-M. Nianga[1,2], and A. Imad[2]

[1]Hautes Etudes d'Ingénieur, 13 rue de Toul, BP 41290, 59014 Lille Cedex, France
[2]Unité de Mécanique de Lille, EA7512, Université de Lille, Villeneuve-d'Ascq, France

Abstract

In this paper, we propose a new technique that is, at least, as efficient as the technique proposed by Dally and Sanford (DS) [3] to determine the stress intensity factor (SIF) in Mode I. This technique relies on the use of a single or two rectangular rosettes with two elements for a three- or four-term representations of the strain field. The strong point of this technique is that regardless of the type of material used the location angle θ and orientation angle α of rectangular rosette are not changing with respect to the Poisson's ratio ν. In addition, the angle θ coincides with the angle α and is equal to $\pm 60°$, which facilitates the use of this technique in the practice. Moreover, a new formulation of the DS approach is presented. Accordingly, general finite element approaches are developed to estimate the extent validity of the three and four-term representations of the strain field for the two techniques. Results of numerical examples show that the present technique can yield a highly accurate value of SIF when the single or two rectangular rosettes are placed within the valid locations. Furthermore, these results show that the proposed technique and the technique of DS give almost the same precision in the measured SIF values.

*Corresponding author at: Unité de Mécanique de Lille, EA7512, Université de Lille, Villeneuve-d'Ascq, France.
tkanit@univ-lille.fr (T. Kanit).

Keywords
Rosette
Strain gage
Stress intensity factor
Mode I
Optimal locations

1 Introduction

In fracture mechanics of stationary and propagating cracks in homogenous materials, the primary focus is generally based on the first singular term in the Williams [1] series expansion, proportional to SIF. More accurate values of SIFs are important in predicting and preventing the fracture of the engineering components. Several experimental techniques have been developed over the years to measure SIFs in cracked bodies, such as the compliance method [2,3], photoelasticity [4–6], caustics [7,8] and strain gage methods [9–16]. Among these experimental techniques, strain gage techniques are the most common methods used to date in experimental stress analysis. This is due to their simplicity and their ease of use in most environments [17]. They can measure surface strains accurately and directly within strain gradient zones, allowing the subsequent determination of SIFs.

Irwin [18] was the first to propose the idea of using strain gages to determine the SIF near the crack tip. For more than two decades thereafter, little progress was made in implementing this idea in practice. The primary reasons for the delay in the development of an appropriate technique are related to several factors such as the local yielding effect at the crack tip of metallic materials, high strain gradients, the complexity of the three-dimensional state of stress at the crack tips and the finite size of the strain gages. To overcome these difficulties, DS [9] were the first to develop a strain gage technique for measuring the static mode I SIF in two-dimensional isotropic bodies. The chief advantage of their technique is that a single strain gage is sufficient to accurately determine the SIF. The accuracy in the determination of the SIF depends on the gage location and orientation relative to the crack tip. Thanks to its simplicity and efficiency, this technique has been widely used by many researchers [19–27] for determination of mode I SIF in different contexts.

Later, Dally and Berger [28] and Dally and Barker [29] extended this technique for determination of the mixed-mode SIFs and dynamic SIF respectively. Shukla et al. [30] and Khanna and Shukla [31] extended the same technique to static and dynamic cracks of orthotropic composite materials. Berger and Dally [10] proposed a strain gage technique based on many measurements for determining the opening-mode SIF by solving a large number of over deterministic equations. Wei and Zhao [23] developed a method that requires two strain gages to measure the mode I SIF. Kondo et al. [12,32] used ten strain gages to determine the mixed-mode SIFs of a sharp notch. Dorogoy and Rittle [13] proposed a technique using a three

strain gage rosette for the determination of mixed-mode SIFs. Ricci et al. [14] used two strain gages at two different locations for determining the complex SIF of a bi-material crack. Marur and Tippur [16] also developed a biaxial rosette technique for determining the complex stress intensity factor in bi-material systems. Bürgel et al. [33] have developed a strain gage measuring technique for determining mode II SIF following the ideas introduced by Dally and Sanford. These researchers remarked that since the influence of higher-order terms is not eliminated, a few strain gages should be used, and, an extrapolation should be conducted for obtaining accurate SIF from the strain gages measurements. Accurate calculation of SIF requires more than one strain gage. More recently Pranjol et al. [34] extended the technique of DS to V-notched configurations to measure the mode I notch SIF.

Although some recommendations are available for the radial locations of strain gage techniques in [11,13,31]. But no procedure was mentioned to determine the valid radial locations in this works. In contrast, Sarangi et al. [35–37] presented for the first time a general theoretical methodology based on the finite element analysis to obtain the valid radial locations for the technique of single strain gage proposed by DS. They defined a parameter r_{max} which is the upper bound on the radial location for the strain gage which in turn can be used for locating the optimal or valid radial locations for strain gages. Their results show the importance of knowing the r_{max} value of an experimental specimen before conducting an experiment for the determination of mode I SIF. The same authors [38] also proposed a methodology for obtaining the valid radial locations of the strain gages in order to accurately determine the mixed-mode SIFs. Debaleena Chakraborty et al. [39–41] and Pranjol Paul et al. [42] have extended the methodologies proposed by these authors for orthotropic composite materials and for isotropic body containing a sharp V-notch, respectively. Next, experiments conducted by Sarangi et al. [27,43], Debaleena Chakraborty et al. [44] and Pranjol Paul et al. [34] have shown the effectiveness of these theoretical methodologies and the usefulness of the optimal strain gage locations in accurate measurement of SIFs.

The application of a rectangular rosette comprising two strain gages to determine the K_I was addressed for the first time by DS [9]. These authors advised using a rectangular rosette when the fracture specimen is subjected to a temperature gradient and temperature compensation is important. The rectangular rosette technique proposed by these authors makes it possible to evaluate K_I for a two-term representation of the strain field. The rectangular rosette has also been used by Maleski et al. [25] to determine the T-stress for a two-term representation of the strain field. Marur and Tippur [45] also used a rectangular rosette to measure the radial and hoop strains to determine the interfacial fracture parameters of bi-material and functionally graded materials under impact loading conditions. The rectangular rosette was used by these authors to improve the accuracy of dynamic loading when separate locations could be subjected to different stress conditions.

According to the works mentioned above, the rectangular rosette has the advantage of providing the first two coefficients of the asymptotic expansion at one point

while preserving space. On the other hand, they also have advantage in dynamic loading situations and specimens subjected to temperature gradients. This paper aims to propose a new rectangular rosette technique in order to meet these requirements. Another major advantage of the proposed technique is that the location and orientation of the rosettes do not change with the material properties and can be easily located on the specimen to be tested. This work is a natural extension of the work of DS [9].

The paper is organized as follows: (1) the formulation of the strains $\varepsilon_{x'x'}$ and $\varepsilon_{y'y'}$ at a point $P(r,\theta)$ close to the crack tip in α direction is given explicitly using the first four terms of the generalized Westergaard formulation [46]. (2) A new formulation of the DS technique is presented. The analytic expression of the angle of θ is given as a function of the Poisson's ratio, ν, and a simplified rewrite of the strain expression, $\varepsilon_{x'x'}$, is obtained. Also, the extent of validity of the three- and four-term representation proposed by DS is determined. (3) A new technique is proposed to evaluate the value of SIF using a single or two rectangular rosettes. The basic theoretical formulation for the determination of the extent of validity of the three- and four-term representation is also presented. (4) The analysis is followed by numerical examples of an edge crack in a finite plate subjected to mode I loading conditions. The main results are then discussed and followed with a concluding section.

2 Theoretical formulation

We assume that the material of the cracked specimen is homogeneous, linear elastic, isotropic and subjected to small deformations. The near field strain equations are obtained using the generalized Westergaard approach proposed by [46]. The modified Airy stress function in this approach is given by [47]

$$\phi = \Re\left(\overline{\overline{Z}}(z)\right) + y\Im\left(\overline{Z}(z)\right) + y\Im\left(\overline{Y}(z)\right) \tag{1}$$

where

$$Z = \frac{d}{dz}\overline{Z}(z) = \frac{d^2}{dz^2}\overline{\overline{Z}}(z), \quad Y = \frac{d}{dz}\overline{Y}(z), \quad z = x + iy$$

and the complex analytic functions $Z(z)$ and $Y(z)$ are defined as

$$Z(z) = \sum_{n=0}^{\infty} A_n z^{n-\frac{1}{2}} \quad \text{and} \quad Y(z) = \sum_{m=0}^{\infty} B_m z^m \tag{2}$$

which are series type functions containing an infinite number of real constants $(A_0, A_1, A_2, \ldots, A_\infty;\ B_0, B_1, B_2, \ldots, B_\infty)$ that can be determined using geometry and boundary conditions of a given problem. The stress components for the entire domain are represented by DS [9] as

$$\begin{aligned} \sigma_{xx} =& \Re(Z) - y\left[\Im(Z') + \Im(Y')\right] + 2\Re(Y) \\ \sigma_{yy} =& \Re(Z) + y\left[\Im(Z') + \Im(Y')\right] \\ \tau_{xy} =& -y\left[\Re(Z') + \Re(Y')\right] - \Im(Y) \end{aligned} \tag{3}$$

Assuming plane stress conditions, equations for strain field are given as

$$\begin{aligned} E\varepsilon_{xx} =& f_1 \Re(Z) - f_2 y \left[\Im(Z') + \Im(Y')\right] + 2\Re(Y) \\ E\varepsilon_{yy} =& f_1 \Re(Z) + f_2 y \left[\Im(Z') + \Im(Y')\right] - 2\nu\Re(Y) \\ E\gamma_{xy} =& -2 f_2 \left[y\left(\Re(Z') + \Re(Y')\right) + \Im(Y)\right] \end{aligned} \tag{4}$$

where the parameters f_1 and f_2 are given by, $f_1 = 1 - \nu$ and $f_2 = 1 + \nu$.

Substitution of $Z(z)$ and $Y(z)$ and their derivatives in Eqs. (4) gives exact representation of strain field with infinite number of unknown terms A_n and B_m. It is assumed that the strain field around the crack tip can be sufficiently represented a truncated series of four terms only ($n = 0, 1$ and $m = 0, 1$) with unknown terms A_0, A_1, B_0 and B_1. The four-term representation of strain field is therefore,

$$\begin{aligned} E\varepsilon_{xx} =& \cos(\theta/2)\left[f_1 - f_2 \sin(\theta/2)\sin(3/2\,\theta)\right] A_0 r^{-\frac{1}{2}} + 2B_0 r^0 + \\ & \cos(\theta/2)\left[f_1 + f_2 \sin^2(\theta/2)\right] A_1 r^{\frac{1}{2}} + 2\cos(\theta) B_1 r \end{aligned} \tag{5}$$

$$\begin{aligned} E\varepsilon_{yy} =& \cos(\theta/2)\left[f_1 + f_2 \sin(\theta/2)\sin(3/2\,\theta)\right] A_0 r^{-\frac{1}{2}} - 2\nu B_0 r^0 + \\ & \cos(\theta/2)\left[f_1 - f_2 \sin^2(\theta/2)\right] A_1 r^{\frac{1}{2}} - 2\nu\cos(\theta) B_1 r \end{aligned} \tag{6}$$

$$E\gamma_{xy} = f_2 \sin(\theta)\left[\cos(3/2\,\theta) A_0 r^{-\frac{1}{2}} - \cos(\theta/2) A_1 r^{\frac{1}{2}} - 4B_1 r\right] \tag{7}$$

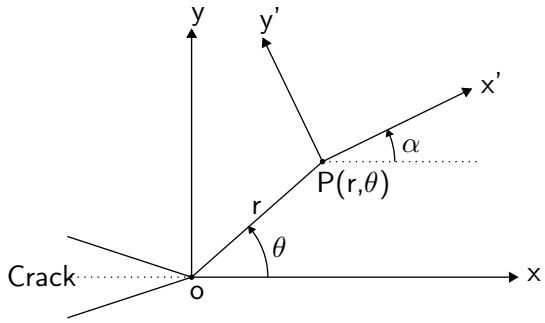

Fig. 1. Strain gage location and orientation.

The strains relative to a rotated coordinate system (x', y') with its origin at an arbitrary point P located by r and θ (Fig. 1) are determined from the first invariant of strain

$$\varepsilon_{x'x'} + \varepsilon_{y'y'} = \varepsilon_{xx} + \varepsilon_{yy} \tag{8}$$

and the complex form of the strain-transformation equation

$$\varepsilon_{y'y'} - \varepsilon_{x'x'} + i\gamma_{x'y'} = \left(\varepsilon_{yy} - \varepsilon_{xx} + i\gamma_{xy}\right) e^{2i\alpha} \tag{9}$$

Substituting Eqs. (5)-(7) into Eqs. (8) and (9) leads to

$$2G\varepsilon_{x'x'} = \left[\kappa\cos(\theta/2) + \frac{1}{2}\sin(\theta)\left(\cos(3/2\,\theta)\sin(2\alpha) - \sin(3/2\,\theta)\cos(2\alpha)\right)\right] A_0 r^{-\frac{1}{2}} + \left[\kappa + \cos(2\alpha)\right] B_0 + \cos(\theta/2)\left[\kappa + \sin^2(\theta/2)\cos(2\alpha) - \frac{1}{2}\sin(\theta)\sin(2\alpha)\right] A_1 r^{\frac{1}{2}} + \left[\kappa\cos(\theta) + \cos(\theta)\cos(2\alpha) - 2\sin(\theta)\sin(2\alpha)\right] B_1 r \tag{10}$$

$$2G\varepsilon_{y'y'} = \left[\kappa\cos(\theta/2) - \frac{1}{2}\sin(\theta)\left(\cos(3/2\,\theta)\sin(2\alpha) - \sin(3/2\,\theta)\cos(2\alpha)\right)\right] A_0 r^{-\frac{1}{2}} + \left[\kappa - \cos(2\alpha)\right] B_0 + \cos(\theta/2)\left[\kappa - \sin^2(\theta/2)\cos(2\alpha) + \frac{1}{2}\sin(\theta)\sin(2\alpha)\right] A_1 r^{\frac{1}{2}} + \left[\kappa\cos(\theta) - \cos(\theta)\cos(2\alpha) + 2\sin(\theta)\sin(2\alpha)\right] B_1 r \tag{11}$$

where the parameter κ is given by, $\kappa = f_1/f_2$. By applying the standard definition of mode I SIF K_I, it can be easily shown that A_0 is related to the SIF by the relation

$$K_I = \sqrt{2\pi} A_0 \tag{12}$$

To make effective use of strain gage, it is necessary to determine its optimum location relative to the crack tip. Three parameters must be examined when mounting a gage near a crack tip, i.e. the location in relation to the crack tip (r, θ), and the orientation angle α.

2.1 DS approach formulation

The orientation angle α is usually chosen such as to eliminate the effect of the B_0 term. It can be observed in Eq. (12) that coefficient associated with B_0 term only depends on ν and α. The effect of the B_0 term on the strain gage reading is completely eliminated if α is chosen as

$$\alpha = \pm\frac{1}{2}\arccos(-\kappa) \tag{13}$$

Similarly, the coefficient of the term A_1 can also be made zero if the angle θ is selected as

$$\tan(\theta/2) = -\cot(2\alpha) \tag{14}$$

that is to say if the relation between θ and α is such that

$$\theta = 4\alpha \mp 180^\circ \tag{15}$$

Substituting Eq. (13) into Eq. (15) gives

$$\theta = \pm 2\arccos(-\kappa) \mp 180^\circ = \pm 2\arcsin(\kappa) \tag{16}$$

Now, substituting α and θ as defined by Eq. (13) and Eq. (16), respectively, into Eq. (12), one obtains the following relation

$$G\varepsilon_{x'x'} = \kappa\left(1-\kappa^2\right)^{\frac{3}{2}} A_0 r^{-\frac{1}{2}} - 2\kappa\left(1-\kappa^2\right) B_1 r \tag{17}$$

Substituting Eq. (12) into Eq. (17), Eq. (17) can be rewritten as

$$K_I(r) = K_I - C_1 r^{\frac{3}{2}} \tag{18}$$

where

$$K_I(r) = \frac{G\sqrt{2\pi r}\ \varepsilon_{x'x'}}{\kappa\,(1-\kappa^2)^{\frac{3}{2}}} \tag{19}$$

and

$$C_1 = \frac{2\sqrt{2\pi}B_1}{(1-\kappa^2)^{\frac{1}{2}}} \tag{20}$$

In what follows, we present the two cases proposed by DS [9] to determine K_I, as well as the methodologies to be used to determine the extent of their valid region. The first case requires the use of a single gage for a three-term representation and the second case requires the use of two gages for a four-term representation.

2.1.1 Case of a single gage

For a three-term representation, a single gage can be used to provide the data necessary to determine K_I. In this case, Eq. (18) reduces to

$$K_I = \frac{G\sqrt{2\pi r}\ \varepsilon_{x'x'}}{\kappa\,(1-\kappa^2)^{\frac{3}{2}}} \tag{21}$$

Now, if we consider the example of an aluminum specimen with $\nu = 1/3$. Eqs. (13) and (16) give $\alpha = \theta = \pm 60°$, in this case the strain $\varepsilon_{x'x'}$ is equivalent to the radial strain ε_{rr}. Then, the substitution $G = 3/8\,E$ and $\kappa = 1/2$ into Eq. (21) give the first formula proposed by DS [9]

$$K_I = E\sqrt{(8/3)\pi r}\ \varepsilon_{rr} \tag{22}$$

Eq. (21) accurately determines K_I up to a radial distance $r^{DS}_{1,max}$ which assures stable values of K_I. Thus, $r^{DS}_{1,max}$ is the point that separates the region of stable behavior from unstable behavior in the plot of the right-hand side of Eq. (21). The $r^{DS}_{1,max}$ can ~~also~~ be determined by the methodology proposed by Sarangi et al. [35–37] for determining the extent of validity of the three-term solution (Eq. (21)). Eq. (21) accurately determines $\varepsilon_{x'x'}$ up to a radial distance of $r^{DS}_{1,max}$ and it can be written as

$$\varepsilon_{x'x'} = \frac{D_1}{\sqrt{r}} \tag{23}$$

where $D_1 = \frac{\kappa\left(1-\kappa^2\right)^{\frac{3}{2}} K_I}{G\sqrt{2\pi}}$ is a constant. Taking logarithm on both sides of Eq. (23)

$$\ln(\varepsilon_{x'x'}) = -\frac{1}{2}\ln(r) + \ln(D_1) \tag{24}$$

Eq. (24) is valid until a radial distance of $r^{DS}_{1,max}$ along the gage line which makes an angle $\theta = \pm 2\arcsin(\kappa)$ with the axis of crack. Thus, a log-log plot of Eq. (24) is a straight line of slope equals to -0.5, with an intercept of $\ln(D_1)$. Theoretically, the straight-line

property breaks for $r > r^{DS}_{1,max}$, because then more than three terms are needed in Eq. (21) to estimate $\varepsilon_{x'x'}$. Using Eq. (24), the value of $r > r^{DS}_{1,max}$ can be accurately estimated. Also, to avoid 3D effects, the minimum radial distance r_{min} should be greater than half the thickness of the plate [29]. Therefore, the valid radial locations for a single gage can now be stated as

$$r_{min} \leq r \leq r^{DS}_{1,max} \tag{25}$$

Thus, by placing a single gage as shown in Fig. 1 oriented at an angle of $\alpha = \pm\frac{1}{2}\arccos(-\kappa)$ at a radial distance r between r_{min} and $r^{DS}_{1,max}$ along the gage line at an angle of $\theta = \pm 2\arcsin(\kappa)$, the measured strain $\varepsilon_{x'x'}$ can be used to obtain K_I using Eq. (21).

2.1.2 Case of two gages

It is possible to obtain the data necessary to determine K_I from a four-term representation by using two gages. Now, if we place two gages G_A and G_B with the same values of α and θ as defined by Eqs. (13) and (15), their respective positions r_A and r_B, and their respective strain readings $(\varepsilon_{x'x'})_{r=r_A}$ and $(\varepsilon_{x'x'})_{r=r_B}$ can be used to solve Eq. (18) for K_I. Thus, when solving Eq. (18) for K_I, using data obtained from gages G_A and G_B one can write

$$K_I = \frac{K_I(r_A)}{1 - \left(\frac{r_A}{r_B}\right)^{3/2}} + \frac{K_I(r_B)}{1 - \left(\frac{r_B}{r_A}\right)^{3/2}} \tag{26}$$

where $K_I(r_A)$ and $K_I(r_B)$ are the SIFs calculated in the case of a three-term representation from Eq. (21).

The maximum radial distance $r^{DS}_{2,max}$ of the extent of validity of the four-term representation can be obtained by comparing the two quantities on the left-hand side and right-hand side of Eq. (18). The quantity on the left-hand side of Eq. (18) is computed from the $\varepsilon_{x'x'}$ value evaluated at radial locations in the $\alpha = \pm\frac{1}{2}\arccos(-\kappa)$ direction along the gage line $\theta = \pm 2\arcsin(\kappa)$. The accurate value of K_I can be obtained using the best fit regression of the plot of the right-hand side quantities of Eq. (18). The $r^{DS}_{2,max}$ is the point of deviation of the curve of the right-hand side of Eq. (18) from the curve of the left-hand side. Consequently, the valid radial locations for the two gages are given by

$$r_{min} \leq r_A < r_B \leq r^{DS}_{2,max} \tag{27}$$

By sticking two gages G_A and G_B as indicated in Fig. 1 oriented at an angle of $\alpha = \pm\frac{1}{2}\arccos(-\kappa)$ at radial distances r_A and r_B between r_{min} and $r^{DS}_{2,max}$ along the gage line $\theta = \pm 2\arcsin(\kappa)$, the measured strains $(\varepsilon_{x'x'})_{r=r_A}$ and $(\varepsilon_{x'x'})_{r=r_B}$ can be used to obtain K_I using Eq. (26).

2.2 Proposed technique

Now, if the angle θ coincides with the angle α, the strains $\varepsilon_{x'x'}$ and $\varepsilon_{y'y'}$ are equivalent to radial strain ε_{rr} and tangential strain $\varepsilon_{\theta\theta}$, respectively. For this case, Eqs. (12) and (11)

give respectively

$$2G\varepsilon_{rr} = \left[\kappa\cos(\theta/2) + \frac{1}{4}\left(\cos(\theta/2) - \cos(3/2\,\theta)\right)\right] A_0 r^{-\frac{1}{2}} + \left[\kappa + \cos(2\theta)\right] B_0 + \left[\kappa\cos(\theta/2) - \frac{1}{4}\left(\cos(\theta/2) - \cos(5/2\,\theta)\right)\right] A_1 r^{\frac{1}{2}} + \left[\kappa\cos(\theta) - \frac{1}{2}\left(\cos(\theta) - 3\cos(3\theta)\right)\right] B_1 r \tag{28}$$

$$2G\varepsilon_{\theta\theta} = \left[\kappa\cos(\theta/2) - \frac{1}{4}\left(\cos(\theta/2) - \cos(3/2\,\theta)\right)\right] A_0 r^{-\frac{1}{2}} + \left[\kappa - \cos(2\theta)\right] B_0 + \left[\kappa\cos(\theta/2) + \frac{1}{4}\left(\cos(\theta/2) - \cos(5/2\,\theta)\right)\right] A_1 r^{\frac{1}{2}} + \left[\kappa\cos(\theta) + \frac{1}{2}\left(\cos(\theta) - 3\cos(3\theta)\right)\right] B_1 r \tag{29}$$

Using Eqs. (28) and (29), the term B_0 can be completely eliminated by superposing ε_{rr} with an appropriate fraction of $\varepsilon_{\theta\theta}$ as

$$\frac{2G}{\kappa}\left([\kappa - \cos(2\theta)]\varepsilon_{rr} - [\kappa + \cos(2\theta)]\varepsilon_{\theta\theta}\right) = 2\cos^3(\theta/2)[1 - 8\sin^2(\theta/2)]A_0 r^{-\frac{1}{2}} - 2\cos^3(\theta/2)[1 - 4\sin^2(\theta/2)]A_1 r^{\frac{1}{2}} - 4\sin(\theta)\sin(2\theta)B_1 r \tag{30}$$

Considering Eq. (30), the term A_1 can be eliminated if

$$\theta = \pm 60^\circ \tag{31}$$

When substituting Eq. (31) into Eq. (30), one can obtain the following relation

$$\frac{G}{\kappa}\left[(2\kappa + 1)\varepsilon_{rr} - (2\kappa - 1)\varepsilon_{\theta\theta}\right] = \frac{3\sqrt{3}}{4} A_0 r^{-\frac{1}{2}} - 3B_1 r \tag{32}$$

Substituting Eq. (12) into Eq. (32), Eq. (32) can be rewritten as

$$K_I(r) = K_I - C_2 r^{\frac{3}{2}} \tag{33}$$

where

$$K_I(r) = \frac{4G\sqrt{2\pi r}}{3\sqrt{3}\kappa}\left[(2\kappa + 1)\varepsilon_{rr} - (2\kappa - 1)\varepsilon_{\theta\theta}\right] \tag{34}$$

and

$$C_2 = \frac{4\sqrt{2\pi}B_1}{\sqrt{3}} \tag{35}$$

Two cases will be presented here to determine K_I. The first case requires the use of a single rectangular rosette for a three-term representation and the second case requires the use of two rectangular rosettes for a four-term representation. In both cases, a methodology is proposed to determine the extent of the valid region for placing the rectangular rosettes in order to accurately determine the K_I.

2.2.1 Case of a single rectangular rosette

A single rectangular rosette can be used to provide the data necessary to determine K_I for a three-term representation. If only the first three terms are retained in the series representation, Eq. (33) reduces to

$$K_I = \frac{4G\sqrt{2\pi r}}{3\sqrt{3}\kappa}\left[(2\kappa+1)\varepsilon_{rr} - (2\kappa-1)\varepsilon_{\theta\theta}\right] \tag{36}$$

Now, if we consider again the example of an aluminum specimen with $\nu = 1/3$, Eq. (36) reduces to first formula proposed by DS [9]

$$K_I = E\sqrt{(8/3)\pi r}\ \varepsilon_{rr} \tag{37}$$

It is clear from Eq. (37) that the strain measured by the radially aligned gage is sufficient to provide the data necessary for the evaluation of the value K_I.

Eq. (36) accurately determines K_I up to a radial distance $r^{PT}_{1,max}$, which corresponds to the extent of the valid region in which the strains can be accurately represented by the series of three-term strains. Thus, $r^{PT}_{1,max}$ is the point that separates the region of stable behavior from unstable behavior in the plot of the right-hand side of Eq. (36). Following the methodology proposed by Sarangi et al. [35–37] for determining $r^{PT}_{1,max}$, Eq. (36) can be written as

$$(2\kappa+1)\varepsilon_{rr} - (2\kappa-1)\varepsilon_{\theta\theta} = \frac{D_2}{\sqrt{r}} \tag{38}$$

where $D_2 = \frac{3\sqrt{3}\kappa K_I}{4\sqrt{2\pi}G}$ is a constant. Taking logarithm on both sides of Eq. (38)

$$\ln\left[(2\kappa+1)\varepsilon_{rr} - (2\kappa-1)\varepsilon_{\theta\theta}\right] = -\frac{1}{2}\ln(r) + \ln(D_2) \tag{39}$$

Eq. (36) is valid until a radial distance of $r^{PT}_{1,max}$ along the rosette line $\theta = 60°$. Thus, a log-log plot of Eq. (36) is a straight line of slope equals to -0.5, with an intercept of $\ln(D_2)$. Using Eq. (36), the value of $r^{PT}_{1,max}$ can be accurately estimated and the valid radial locations for a single rectangular rosette can now be stated as

$$r_{min} \le r \le r^{PT}_{1,max} \tag{40}$$

By positioning a single rectangular rosette as shown in Fig. 1 at a radial distance r between r_{min} and $r^{PT}_{1,max}$ along the gage line $\theta = \pm 60°$, the measured strains ε_{rr} and $\varepsilon_{\theta\theta}$ can be used to obtain K_I using Eq. (36).

2.2.2 Case of two rectangular rosettes

Now, if we consider two rectangular rosettes R_A and R_B installed along the $\theta = 60°$ line, their respective positions r_A and r_B, and their respective strain readings $((\varepsilon_{rr})_{r=r_A}$, $(\varepsilon_{\theta\theta})_{r=r_A})$ and $((\varepsilon_{rr})_{r=r_B}$, $(\varepsilon_{\theta\theta})_{r=r_B})$ can be used to solve Eq. (33) for K_I. Thus, when solving Eq. (33) for K_I, using data obtained from rectangular rosettes R_A and R_B one can write

$$K_I = \frac{K_I(r_A)}{1 - \left(\frac{r_A}{r_B}\right)^{3/2}} + \frac{K_I(r_B)}{1 - \left(\frac{r_B}{r_A}\right)^{3/2}} \tag{41}$$

where $K_I(r_A)$ and $K_I(r_B)$ are the SIFs calculated in the case of a three-term representation from Eq. (36).

Following the methodology adopted in section 2.1.2, the maximum radial distance $r^{PT}_{2,max}$ can be obtained by comparing the two quantities on the left-hand side and right-hand side of Eq. (33). The $r^{PT}_{2,max}$ is the point of deviation of the plot of the right-hand side of Eq. (33) from the plot of the left-hand side. Consequently, the valid radial locations for the two rectangular rosettes are given by

$$r_{min} \leq r_A < r_B \leq r^{PT}_{2,max} \tag{42}$$

Thus, by placing two rectangular rosettes R_A and R_B as indicated in Fig. 1 at radial distances r_A and r_B between r_{min} and $r^{PT}_{2,max}$ along the gage line $\theta = \pm 60°$, the measured strains $((\varepsilon_{rr})_{r=r_A}, (\varepsilon_{\theta\theta})_{r=r_A})$ and $((\varepsilon_{rr})_{r=r_B}, (\varepsilon_{\theta\theta})_{r=r_B})$ can be used to obtain K_I using Eq. (41).

3 Numerical examples and discussions

In this section, numerical examples have been performed using ABAQUS software to validate the rectangular rosette technique proposed in section 2.2. For this purpose, finite width and finite height edge cracked plates subjected to uniform tensile stress are considered. Due to symmetry, only half of the plate is modeled, as shown in Fig. 2(a). The width $b = 100$ mm and the half-height $h = 100$ mm of the plate are fixed in all configurations considered in this study. We assume plane stress conditions, an applied stress value of $\sigma = 1$ MPa, a Young's modulus of $E = 210$ GPa and a Poisson's ratio of $\nu = 0.3$. We generate different configurations, with different values of the crack length to width ratio a/b ranging from 0.1 to 0.9 in steps of 0.1. To assure the highest accuracy in the numerical analyses, more refined meshes were used to discretize the area around the crack tip; see Fig. 2(b).

3.1 Numerical determination of r_{max}

3.1.1 Procedure for determination of $r^{DS}_{1,max}$

According to the technique proposed by DS [9], the single gage must be placed at a suitable location on the gage line $\theta = 65.16°$ in $\alpha = 61.29°$ direction to measure the linear strain $\varepsilon_{x'x'}$. In order to numerically simulate the strain gage based determination of K_I following this technique, strain values $\varepsilon_{x'x'}$ at nodes along the gage line are considered to be strain gage readings. Using these strain values, K_I can be calculated from Eq. (21). The radial distance $r^{DS}_{1,max}$ which assures stable values of K_I is obtained from the procedure devised by Sarangi et al. [35–37]. To ensure the best fit curves in determining $r^{DS}_{1,max}$, the first four nodes are discarded. Fig. 3 shows the plots of $\ln(\varepsilon_{x'x'})$ versus $\ln(r)$. Following this procedure, straight lines having slope of -0.5 are superposed onto the plots of $\ln(\varepsilon_{x'x'})$. It can be clearly seen in Fig. 3 that both the initial straight line portion of the plots and superposed lines are congruent to each other up to a certain radial distance and the numerical results deviate from the superposed line thereafter. This is observed in plots for all values of a/b. The point of deviation or $r^{DS}_{1,max}$ is evaluated as the value

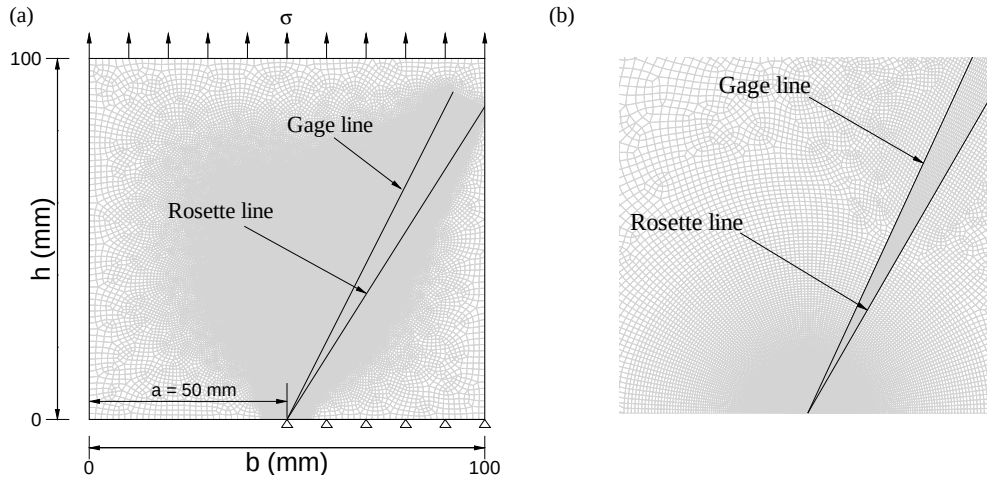

Fig. 2. (a) Geometry of finite edge cracked plate subjected to mode I loading conditions and typical mesh used in the present investigation for finite element analysis, (b) enlarged views at the crack tips corresponding to meshes in (a).

of the radius at which the error reaches 0.5%. Estimated values of the $r_{1,max}^{DS}$ are also presented in Table 1. The results in Table 1 show that the value of $r_{1,max}^{DS}$ increases with the increase of the crack length until reaching a maximum value of 17.14 mm at $a/b = 0.5$, then decreases with the increase in the length of the crack. A similar trend has been reported by Sarangi et al. [35–37]. Fig. 4 illustrates this variation of $r_{1,max}^{DS}$ with a/b. It can be observed also from the results of Table 1 that when the crack tip approaches of the right and left boundary of the cracked plate, the $r_{1,max}^{DS}$ values are very small, which makes it difficult to accurately measure the value of K_I using the technique of the single gage proposed by DS [9].

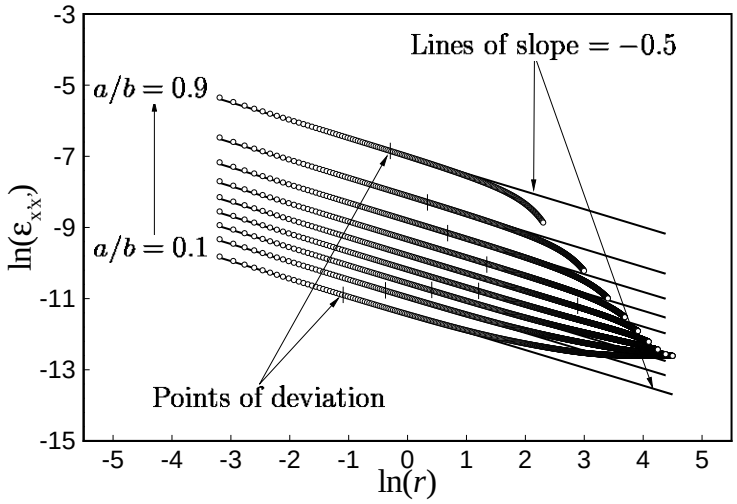

Fig. 3. Variations of $\ln(\varepsilon_{x'x'})$ with $\ln(r)$ along the gage line $\theta = 65.16°$ for different a/b ratios.

Table 1
Variations of $r_{1,max}^{DS}$, $r_{2,max}^{DS}$, $r_{1,max}^{PT}$ and $r_{2,max}^{PT}$ with a/b.

	Proposed technique					DS technique				
	Single rosette		Two rectangular rosettes			Single gage		Two gages		
a/b	$r_{1,max}^{PT}$ (mm)	$r_{1,max}^{PT}/b$	$r_{2,max}^{PT}$ (mm)	$r_{2,max}^{PT}/b$	$r_{2,max}^{PT}/r_{1,max}^{PT}$	$r_{1,max}^{DS}$ (mm)	$r_{1,max}^{DS}/b$	$r_{2,max}^{DS}$ (mm)	$r_{2,max}^{DS}/b$	$r_{2,max}^{DS}/r_{1,max}^{DS}$
0.1	0.37	0.0037	2.83	0.0283	7.645	0.34	0.0034	2.94	0.0294	8.763
0.2	0.77	0.0077	5.63	0.0563	7.288	0.69	0.0069	6.09	0.0609	8.856
0.3	1.67	0.0167	8.49	0.0819	4.486	1.51	0.0151	8.90	0.0890	5.904
0.4	3.66	0.0366	11.84	0.1184	3.239	3.36	0.0336	13.63	0.1363	4.054
0.5	14.52	0.1452	18.26	0.1826	1.258	17.14	0.1714	19.38	0.1938	1.131
0.6	3.84	0.0384	16.96	0.1596	4.157	3.84	0.0384	18.96	0.1896	4.937
0.7	1.97	0.0197	14.59	0.1459	7.390	1.97	0.0197	15.08	0.1508	7.639
0.8	1.21	0.0121	10.64	0.1064	8.765	1.21	0.0121	12.02	0.1202	9.903
0.9	0.76	0.0076	6.95	0.0695	9.184	0.75	0.0075	8.18	0.818	10.968

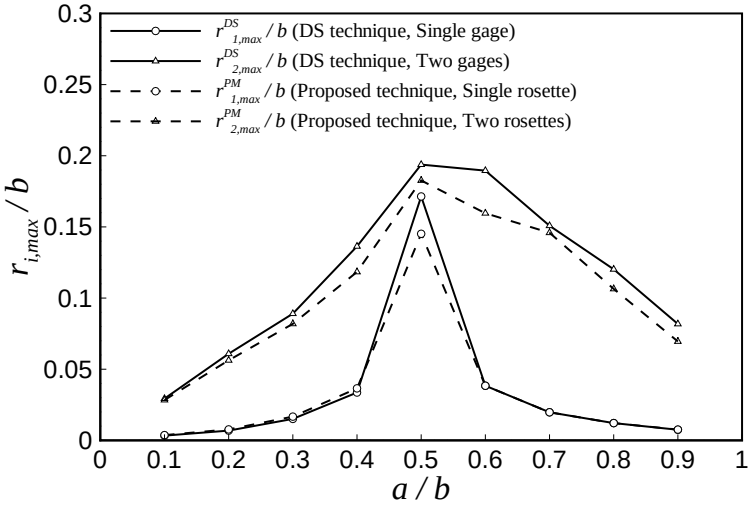

Fig. 4. Variations of $r_{1,max}^{DS}$, $r_{2,max}^{DS}$, $r_{1,max}^{PT}$ and $r_{2,max}^{PT}$ with a/b.

3.1.2 Procedure for determination of $r_{2,max}^{DS}$

Following the procedure described in Section 2.1.2 to estimate the extent of the four-term representation or $r_{2,max}^{DS}$, the quantity on the left-hand side of Eq. (18) is computed from the $\varepsilon_{x'x'}$ values evaluated at radial locations in the $\alpha = 61.29°$ direction along the gage line $\theta = 65.16°$. Fig. 5(a)-(c) show the plot of the left-hand side quantity of Eq. (18) versus radial distance r and its best fit for $a/b = 0.2$, 0.5 and 0.7, respectively. To ensure the best fit curves in determining $r_{2,max}^{DS}$, all the nodes lower than 0.25 mm are discarded. The estimated value of the $r_{2,max}^{DS}$ corresponding to the point of deviation between the plot of the left-hand side quantity of Eq. (18) and its best fit along the gage line is marked in Fig. 5(a)-(c) as per the procedure described above. The radial distance $r_{1,max}^{DS}$ obtained from the log-log procedure and which ensure stable values of K_I for a three-term representation is also marked in these figures. The $r_{2,max}^{DS}$ values are extracted for all a/b configurations. Then, they are tabulated in Table 1 and plotted versus a/b in Fig. 4. It can be observed from Table 1 that the ratio $r_{2,max}^{DS}/r_{1,max}^{DS}$ decreases with the increase of a/b until reaching a minimum value of 1.13 at $a/b = 0.5$, then increases with the increase of a/b. The $r_{2,max}^{DS}$ is 8.76 times wider than $r_{1,max}^{DS}$ at $a/b = 0.1$, which is a value close to the left boundary of the cracked plate and 10.97 times wider at $a/b = 0.9$, which is a value close to the right boundary of the cracked plate. Thus, the use of the technique of two gages proposed by DS is a good solution when the crack tip is near the right and left boundary of the cracked plate.

3.1.3 Procedure for determination of $r_{1,max}^{PT}$

According to the proposed technique of the single rectangular rosette described in Section 2.2.1, a single rectangular rosette is to be placed at an appropriate location along the rosette line $\theta = 60°$ within the estimated $r_{1,max}^{PT}$ in order to measure the linear strains ε_{rr} and $\varepsilon_{\theta\theta}$. From the finite element results, the strains ε_{rr} and $\varepsilon_{\theta\theta}$, as well as the radial distance r are computed for all the nodes along the rosette line. For all a/b configurations, Fig. 6 gives the plots of $\ln\left[(2\kappa+1)\varepsilon_{rr} - (2\kappa-1)\varepsilon_{\theta\theta}\right]$ versus $\ln(r)$ for all the nodal values along the rosette line. To ensure the best fit curves in determining $r_{1,max}^{PT}$, the first four nodes are discarded. It can be seen that the plots consist of a linear behavior part followed by a nonlinear behavior part, as predicted by the theory. The points at which the plots move from linear to nonlinear give the values of $r_{1,max}^{PT}$. Lines of slope -0.5 are superposed on the plots of $\ln\left[(2\kappa+1)\varepsilon_{rr} - (2\kappa-1)\varepsilon_{\theta\theta}\right]$ and considering these lines as being the exact solutions, absolute percentage relative error at all values of radius of these plots are calculated. The $r_{1,max}^{PT}$ are estimated at points where the error is less than 0.5%. The values of the $r_{1,max}^{PT}$ for all a/b configurations are also presented in Table 1 and plotted versus a/b in Fig. 4. Similarly to the results obtained by using the technique of a single gage proposed by DS, the value of $r_{1,max}^{PT}$ increases with the increase of the crack length until reaching a maximum value of 14.52 mm at $a/b = 0.5$, then decreases with the increase in the length of the crack. One can observe in Fig. 4 that the plot of $r_{1,max}^{PT}$ is almost similar to the plot of $r_{1,max}^{DS}$, the difference is very small between the two plots, except at $a/b = 0.5$ where the difference is maximum and equal to 2.62 mm. Note that when the crack tip approaches of the right and left boundary of the cracked plate, the $r_{1,max}^{PT}$ values are also very small, as the case of a single gage proposed by DS.

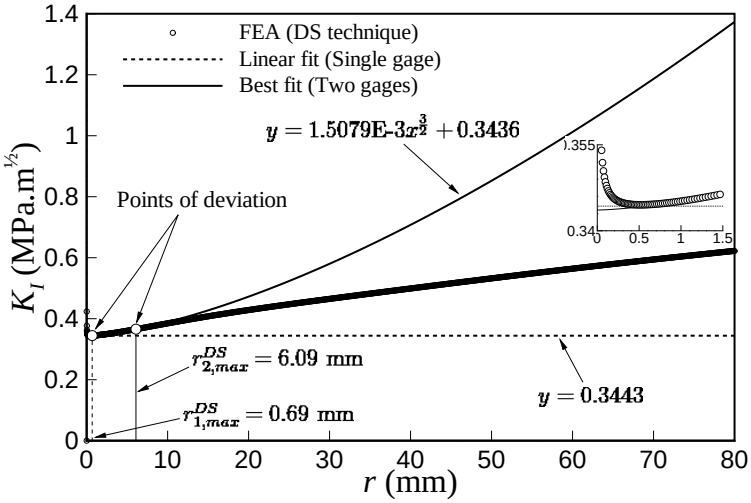

(a)

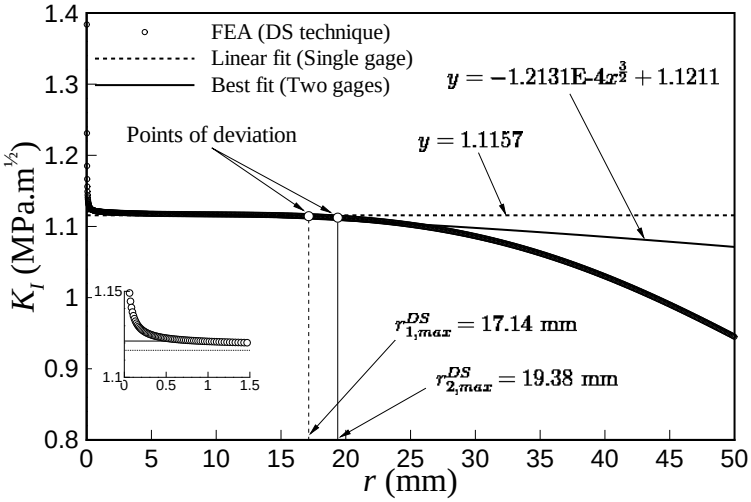

(b)

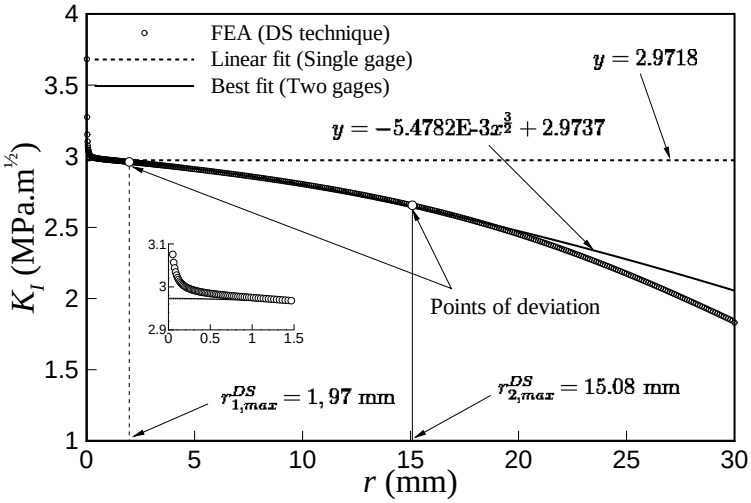

(c)

Fig. 5. Variation of K_I with r along the gage line $\theta = 65.16°$ for (a) $a/b = 0.2$, (b) $a/b = 0.5$ and (c) $a/b = 0.7$.

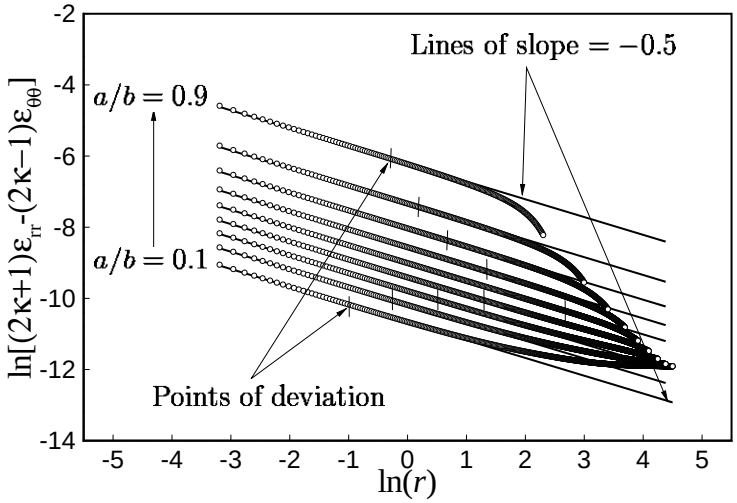

Fig. 6. Variations of $\ln\left[(2\kappa+1)\varepsilon_{rr}-(2\kappa-1)\varepsilon_{\theta\theta}\right]$ with $\ln(r)$ along the rosette line $\theta = 60°$ for different a/b ratios.

3.1.4 Procedure for determination of $r_{2,max}^{PT}$

The same procedure used in the case of two gages was used to determine the extent of validity of Eq. (33) (i.e. the value of $r_{2,max}^{PT}$) in the case of two rectangular rosettes. The quantity on the left-hand side of Eq. (33) is computed from the values of ε_{rr} and $\varepsilon_{\theta\theta}$ evaluated at radial locations along the rosette line $\theta = 60°$. The plot of the left-hand side quantity of Eq. (33) versus radial distance r and its best fit for configurations $a/b = 0.2$, 0.5 and 0.7 are shown in Fig. 7(a)-(c), respectively. The estimated value of the $r_{2,max}^{PT}$ corresponding to the point of deviation between the curve of the measured quantity $\frac{4G\sqrt{2\pi r}}{3\sqrt{3\kappa}}\left[(2\kappa+1)\varepsilon_{rr}-(2\kappa-1)\varepsilon_{\theta\theta}\right]$ and the curve of the form $K_I - C_2 r^{\frac{3}{2}}$ is marked in these figures. In addition, the radial distance $r_{1,max}^{PT}$ obtained from the log-log for a three-term representation is also indicated in these figures. The $r_{2,max}^{PT}$ values are extracted for all a/b configurations and tabulated in Table 1 and plotted versus a/b in Fig. 4. Fig. 4 shows that the curve of $r_{2,max}^{PT}$ followed the same trend of the curve $r_{2,max}^{DS}$. Similarly to the results obtained by using the technique of two gages proposed by DS, the results of Table 1 shows that the ratio $r_{2,max}^{PT}/r_{1,max}^{PT}$ decreases with the increase of a/b until reaching a minimum value of 1.26 at $a/b = 0.5$, then increases with the increase of a/b. The $r_{2,max}^{PT}$ is 7.65 times wider than $r_{1,max}^{PT}$ at $a/b = 0.1$, which is a value close to the left boundary of the cracked plate and 9.18 times wider at $a/b = 0.9$, which is a value close to the right boundary of the cracked plate. The use of the two rectangular rosettes technique proposed is recommended when the crack tip is near the right and left boundary of the cracked plate.

3.2 Validation of the technique

3.2.1 Both cases of single rectangular rosette and single gage

To test the effectiveness of the proposed technique for determining K_I using single rectangular rosette, the radial ε_{rr} and tangential $\varepsilon_{\theta\theta}$ strains values at the nodes along the

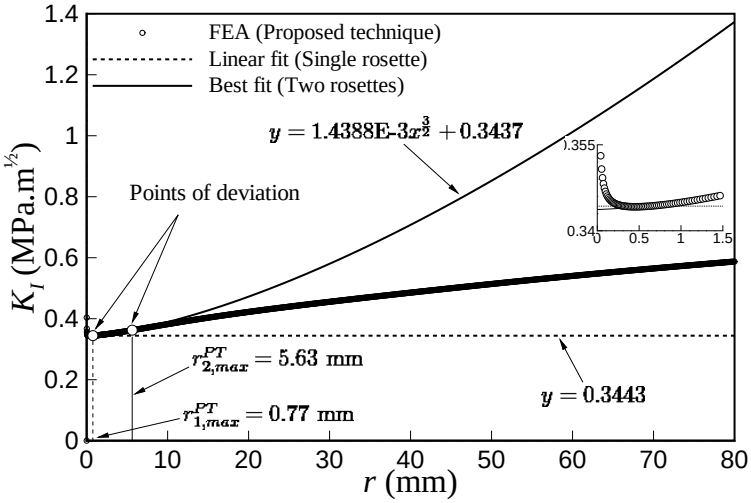

(a)

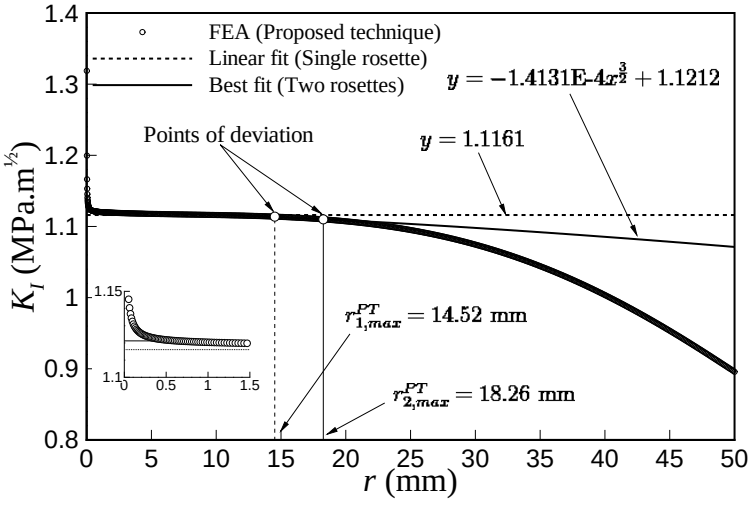

(b)

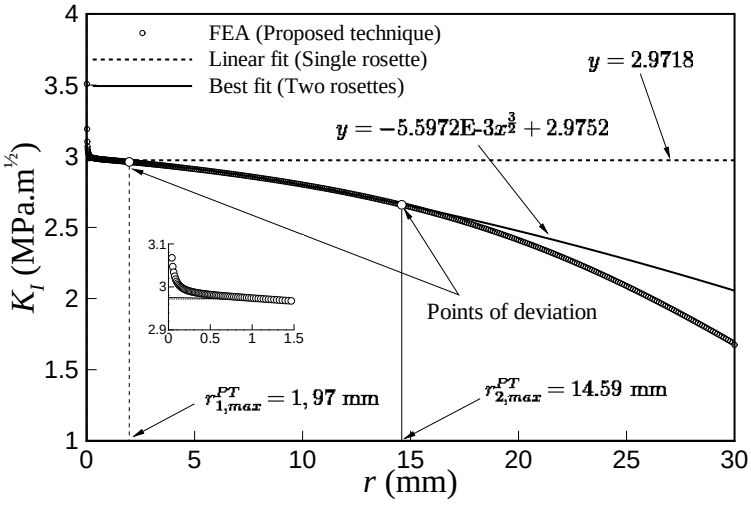

(c)

Fig. 7. Variation of K_I with r along the rosette line $\theta = 60°$ for (a) $a/b = 0.2$, (b) $a/b = 0.5$ and (c) $a/b = 0.7$.

rosette line $\theta = 60^\circ$ are considered as strain rosette readings. Using the ε_{rr} and $\varepsilon_{\theta\theta}$ strains values, K_I have been calculated using Eq. (36). Similarly, in the case of the single gage technique proposed by DS, K_I has been calculated from the $\varepsilon_{x'x'}$ strain values at the nodes along the gage line $\theta = 65.16^\circ$ using Eq. (21). These two techniques are illustrated with the help of the numerical examples for $a/b = 0.2$, 0.5 and 0.7. The values $K_I = 0.3427$, 1.1192 and 2.9749 MPa $\mathrm{m}^{\frac{1}{2}}$ predicted by ABAQUS in the cases of $a/b = 0.2$, 0.5 and 0.7, respectively, are used as reference solutions to test the accuracy of the simulated values of K_I determined employing these two techniques. The absolute percentage relative error of the numerically simulated K_I values is plotted as a function of the radial emplacement r of the rectangular rosette and of the gage in Fig. 8(a) and (b), respectively. It can be observed in these figures that the error in K_I does not exceed 0.5% if the rectangular rosette and the gage are placed inside the valid region i.e., at $r \leq r^{PT}_{1,max}$ and $r \leq r^{DS}_{1,max}$, respectively. On the other hand, when the rectangular rosette and the gage are placed outside the valid region, the error in K_I increases very rapidly with radial location r.

For $a/b = 0.5$ configuration, Table 2 illustrates four different locations of rectangular rosette and of gage along the rosette line $\theta = 60^\circ$ and the gage line $\theta = 65.16^\circ$, respectively. It could be observed that in both the techniques, the error in K_I measurement are very low when the rectangular rosette is placed within $r^{PT}_{1,max}$ and the gage within $r^{DS}_{1,max}$. In both cases 1 and 2 correspond to the optimal locations $r = 5$ and 10 mm, respectively, the error in K_I does not exceed 0.3% for the rectangular rosette and 0.2% for the gage. It was also observed that the error increase rapidly when the rectangular rosette is placed outside $r^{PT}_{1,max}$ and the gage outside $r^{DS}_{1,max}$. In both cases 3 and 4 correspond to the non-optimal locations $r = 25$ and 35 mm, respectively, the error in K_I jumps from a value of $2.16 - 6.98\%$ for the rectangular rosette and a value of $1.5 - 5.09\%$ for the gage. This shows that the location of the rectangular rosette in $r^{PT}_{1,max}$ and of the gage in $r^{DS}_{1,max}$ is very important for a good estimate of K_I. Also, the plots in Fig. 8(a) and (b), and the results in Table 2 conclude that the use of a single rectangular rosette or a single gage gives almost the same accuracy in the measured values of K_I.

Table 2
K_I obtained for four different locations of the rectangular rosette and of the gage ($a/b = 0.5$; $r^{PT}_{1,max} = 14.52$ mm; $r^{DS}_{1,max} = 17.14$ mm; $K_I^{ref} = 1.1192$ MPa$\sqrt{\mathrm{m}}$).

Case	r (mm)	Single rectangular rosette				Single gage		
		ε_{rr}	$\varepsilon_{\theta\theta}$	K_I (MPa.m$^{\frac{1}{2}}$)	Abs. % rel. err.	$\varepsilon_{x'x'}$	K_I (MPa.m$^{\frac{1}{2}}$)	Abs. % rel. err.
1	5	2.6497E-5	5.4683E-6	1.1177	0.13	2.5157E-5	1.1179	0.12
2	10	1.8618E-5	1.4076E-6	1.1161	0.28	1.7775E-5	1.1170	0.20
3	25	1.1409E-5	-3.0196E-6	1.0950	2.16	1.1096E-5	1.1025	1.50
4	35	9.1398E-6	-3.9235E-6	1.0442	6.68	9.0352E-6	1.0622	5.09

3.2.2 Both cases of two rectangular rosettes and two gages

In order to numerically simulate the determination of K_I following the proposed technique of two rectangular rosettes, ε_{rr} and $\varepsilon_{\theta\theta}$ strain values at nodes along rosette line $\theta = 60^\circ$ are considered to be strain rosette readings. Using these strain values, K_I has been calculated using Eq. (41). Similarly, in the case of the two-gage technique proposed by DS, K_I has been calculated from the $\varepsilon_{x'x'}$ strain values at the nodes along the gage line $\theta = 65.16^\circ$ using Eq. (26).

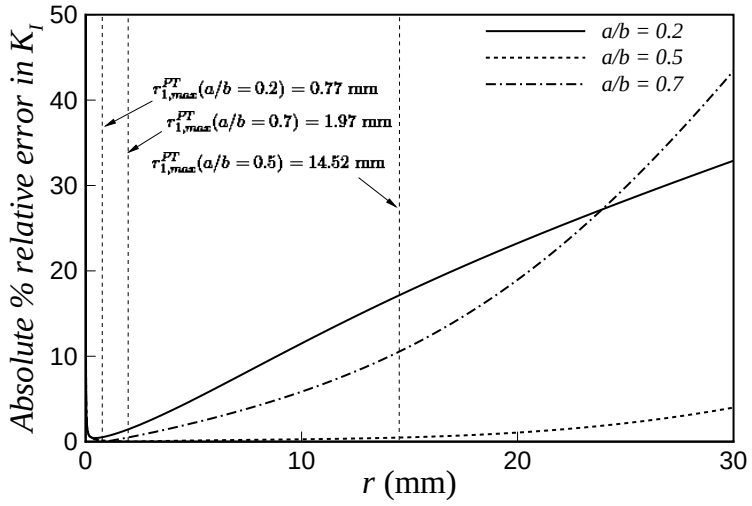

(a)

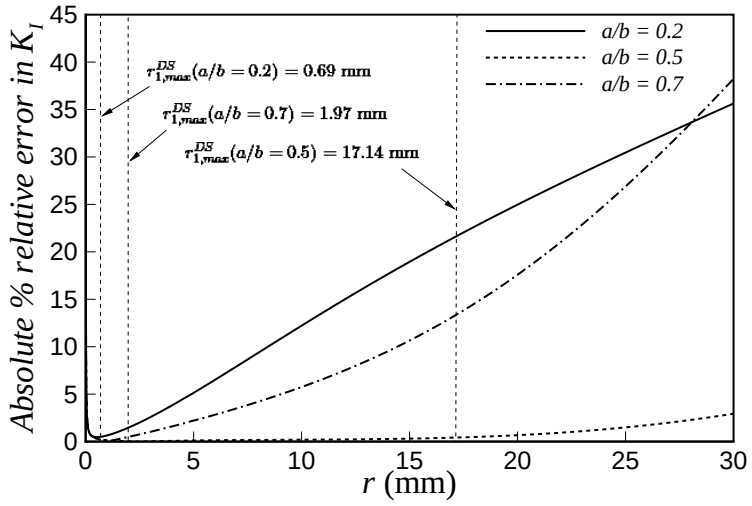

(b)

Fig. 8. Variation of absolute percentage relative error in K_I with the radial position of the rectangular rosette (a) and of the gage (b).

To understand the importance of $r_{2,max}^{PT}$ and $r_{2,max}^{DS}$ on the accuracy of K_I determination, three examples, representing the three possible types of combinations of locations between R_A/G_A and R_B/G_B on the rosette/gage line $\theta = 60°/\theta = 65.16°$ are shown in Tables 3-5 for $a/b = 0.2$, $a/b = 0.5$ and $a/b = 0.7$ configurations, respectively. The first example represents the case where R_A/G_A and R_B/G_B are placed within $r_{2,max}^{PT}/r_{2,max}^{DS}$. The second example represents the case where R_A/G_A is placed within $r_{2,max}^{PT}/r_{2,max}^{DS}$ and R_B/G_B outside $r_{2,max}^{PT}/r_{2,max}^{DS}$. And the third example represents the case where R_A/G_A and R_B/G_B are placed outside $r_{2,max}^{PT}/r_{2,max}^{DS}$. The data of Tables 3-5 shows that the error in K_I is very small when R_A/G_A and R_B/G_B are placed within $r_{2,max}^{PT}/r_{2,max}^{DS}$. The error remains small even when R_B/G_B is placed outside $r_{2,max}^{PT}/r_{2,max}^{DS}$, keeping R_A/G_A within $r_{2,max}^{PT}/r_{2,max}^{DS}$. As mentioned before, this type of combination of locations is not recommended because it does not respect the methodology adopted here to obtain the extent of validity of the four-term representation. The error becomes large when R_B/G_B is placed outside $r_{2,max}^{PT}/r_{2,max}^{DS}$. The results obtained in this study clearly indicate that the location of R_A/G_A and R_B/G_B within $r_{2,max}^{PT}/r_{2,max}^{DS}$ is very important to ensure an accurate measurement of K_I. These results also clearly indicate that the use of two rectangular rosettes or two gages gives almost the same accuracy in the measured values of K_I.

Table 3
K_I obtained for three different locations of two rectangular rosettes and of two gages ($a/b = 0.2$; $r_{1,max}^{PT} = 0.77$ mm; $r_{2,max}^{PT} = 5.63$ mm; $r_{1,max}^{DS} = 0.69$ mm; $r_{2,max}^{DS} = 6.09$ mm; $K_I^{ref} = 0.3427$ MPa$\sqrt{\text{m}}$).

		Proposed technique						DS technique				
				Single rosette		Two rectangular rosettes			Single gage		Two gages	
Case	r_A (mm) / r_B (mm)	ε_{rr}	$\varepsilon_{\theta\theta}$	K_I (MPa.m$^{\frac{1}{2}}$)	Abs. % rel. err.	K_I (MPa.m$^{\frac{1}{2}}$)	Abs. % rel. err.	$\varepsilon_{x'x'}$	K_I (MPa.m$^{\frac{1}{2}}$)	Abs. % rel. err.	K_I (MPa.m$^{\frac{1}{2}}$)	Abs. % rel. err.
1	2.5	1.1725E-5	2.6469E-6	0.3495	1.97	0.3439	0.35	1.1134E-5	0.3498	2.07	0.3440	0.36
	5	8.5121E-6	1.4095E-6	0.3596	4.93			8.1137E-6	0.3605	5.20		
2	5	8.5121E-6	1.4095E-6	0.3596	4.93	0.3473	1.33	8.1137E-6	0.3605	5.20	0.3473	1.32
	10	6.3753E-6	4.9343E-7	0.3822	11.51			6.1234E-6	0.3848	12.28		
3	10	6.3753E-6	4.9343E-7	0.3822	11.51	0.3568	4.10	6.1234E-6	0.3848	12.28	0.3572	4.24
	15	5.4829E-6	1.0078E-7	0.4034	17.71			5.2994E-6	0.4079	19.01		

Table 4
K_I obtained for three different locations of two rectangular rosettes and of two gages ($a/b = 0.5$; $r_{1,max}^{PT} = 14.52$ mm; $r_{2,max}^{PT} = 18.26$ mm; $r_{1,max}^{DS} = 17.14$ mm; $r_{2,max}^{DS} = 19.38$ mm; $K_I^{ref} = 1.1192$ MPa$\sqrt{\text{m}}$).

		Proposed technique						DS technique				
				Single rosette		Two rectangular rosettes			Single gage		Two gages	
Case	r_A (mm) / r_B (mm)	ε_{rr}	$\varepsilon_{\theta\theta}$	K_I (MPa.m$^{\frac{1}{2}}$)	Abs. % rel. err.	K_I (MPa.m$^{\frac{1}{2}}$)	Abs. % rel. err.	$\varepsilon_{x'x'}$	K_I (MPa.m$^{\frac{1}{2}}$)	Abs. % rel. err.	K_I (MPa.m$^{\frac{1}{2}}$)	Abs. % rel. err.
1	5	2.6497E-5	5.4683E-6	1.1177	0.13	1.1187	0.04	2.5157E-5	1.1179	0.12	1.1184	0.07
	15	1.5097E-5	-7.1794E-7	1.1135	0.51			1.4497E-5	1.1157	0.31		
2	15	1.5097E-5	-7.1794E-7	1.1135	0.51	1.1295	0.92	1.4497E-5	1.1157	0.31	1.1272	0.72
	25	1.1409E-5	-3.0196E-6	1.0950	2.16			1.1096E-5	1.1025	1.50		
3	25	1.1409E-5	-3.0196E-6	1.0950	2.16	1.1724	4.75	1.1096E-5	1.1025	1.50	1.1638	3.98
	35	9.1398E-6	-3.9235E-6	1.0442	6.68			9.0352E-6	1.0622	5.09		

4 Conclusion

In the present paper, a two-element rectangular rosette technique for accurate determination of mode I SIF has been proposed. For this purpose, a four-term representation of the strain field was derived from the generalized Westergaard stress functions. The

Table 5
K_I obtained for three different locations of two rectangular rosettes and of two gages ($a/b = 0.7$; $r^{PT}_{1,max} = 1.98$ mm; $r^{PT}_{2,max} = 14.59$ mm; $r^{DS}_{1,max} = 1.97$ mm; $r^{DS}_{2,max} = 15.08$ mm; $K_I^{ref} = 2.9749$ MPa$\sqrt{\text{m}}$).

		Proposed technique						DS technique				
				Single rosette		Two rectangular rosettes			Single gage		Two gages	
Case	r_A (mm) r_B (mm)	ε_{rr}	$\varepsilon_{\theta\theta}$	K_I (MPa.m$^{\frac{1}{2}}$)	Abs. % rel. err.	K_I (MPa.m$^{\frac{1}{2}}$)	Abs. % rel. err.	$\varepsilon_{x'x'}$	K_I (MPa.m$^{\frac{1}{2}}$)	Abs. % rel. err.	K_I (MPa.m$^{\frac{1}{2}}$)	Abs. % rel. err.
1	5	6.8804E-5	9.4875E-6	2.9097	2.19	2.9703	0.15	6.5468E-5	2.9091	2.21	2.9670	0.27
	12	4.1356E-5	-8.9076E-6	2.7451	7.72			3.9972E-5	2.7516	7.51		
2	12	4.1356E-5	-8.9076E-6	2.7451	7.72	3.0279	1.78	3.9972E-5	2.7516	7.51	3.0066	1.07
	19	2.9148E-5	-1.6057E-5	2.4645	17.16			2.8845E-5	2.4986	16.01		
3	19	2.9148E-5	-1.6057E-5	2.4645	17.16	3.1902	7.24	2.8845E-5	2.4986	16.01	3.1249	5.04
	24	2.2548E-5	-1.7434E-5	2.1600	27.39			2.2965E-5	2.2357	24.85		

important property of the proposed technique is that the position and orientation of the rectangular rosette are independent of the physical properties of the material. The use of a single rectangular rosette gives the data necessary for determining K_I in a three-term representation. The use of two rectangular rosettes makes it possible to determine K_I in a four-term representation. To ensure accuracy in the determination of K_I, the extent of validity of the three- and four-term representation is determined. A new formulation of the DS approach has been presented, the analytic expression of the angle of θ is given as a function of the Poisson's ratio, ν, and a simplified rewrite of the strain expression is obtained. The extent of validity of the three- and the four-term representation proposed by DS is also determined. Numerical simulations show that the two techniques give almost the same accuracy in the measured values of K_I. The results of the present investigation show that the proposed two rectangular rosette or two gage DS techniques appear to be practically viable techniques for the configurations where the crack is close to the edges (very small a/b or very large a/b values). For this, it is important to use two rectangular rosettes or two gages to ensure an accurate measurement of K_I. The techniques developed in this study should help the practitioner to choose the technique adapted to each configuration a/b, and to determine the optimal rectangular-rosette or gage locations for accurate experimental measurement of K_I.

References

[1] M.L. Williams, On the stress distribution at the base of a stationary crack, J. Appl. Mech. 24 (1957) 109-114.

[2] R.M. Bonesteel, D.E. Piper, A.T. Davinroy, Compliance and K_I calibration of double cantilever beam (DCB) specimen, Eng. Fract. Mech. 10 (1978) 425-28.

[3] J.C. Newman, Stress-intensity factors and crack-opening displacements for round compact specimens, Int. J. Fract. 17 (1981) 567-578.

[4] E.E. Gdoutos, P.S. Theocaris, A photoelastic determination of mixed-mode stress-intensity factors, Exp. Mech. 18 (1978) 87-96.

[5] T.H. Hyde, N.A. Warrior, An improved method for the determination of photoelastic stress intensity factors using the westergaard stress function, Int. J. Mech. Sc. 32 (1990) 265-273.

[6] M. Mahinfalah, L. Zackery, Photoelastic determination of mixed mode stress intensity factors for sharp reentrant corners, Eng. Fract. Mech. 52 (1995) 639-645.

[7] P.S. Theocaris, Local yielding around a crack tip in plexiglas, J. Appl. Mech. 37 (1970) 409-415.

[8] M. Konsta-Gdoutos, Limitations in mixed-mode stress intensity factor evaluation by the method of caustics, Eng. Fract. Mech. 55 (1996) 371-382.

[9] J.W. Dally, R.J. Sanford, Strain gage methods for measuring the opening mode stress intensity factor, K_I, Exp. Mech. 27 (1987) 381-388.

[10] J.R. Berger, J.W. Dally, An overdeterministic approach for measuring KI using strain gages, Exp. Mech. 28 (1988) 142-145.

[11] J. Wei, J.H. Zhao, A two-strain-gage technique for determining mode I stress intensity factor, Theor. Appl. Fract. Mech. 28 (1997) 135-140.

[12] T. Kondo, Y. Kurabe, T. Sasaki, T. Kurahashi, Y. Miyashita, Use of strain gages for determining generalized stress intensity factors of sharp V-notched plates under transverse bending, Eng. Fract. Mech. 124-125 (2014) 248-261.

[13] A. Dorogoy, D. Rittel, Optimum location of a three strain gauge rosette for measuring mixed mode stress intensity factors, Eng. Fract. Mech. 75 (2008) 4127-4139.

[14] V. Ricci, A. Shukla, R.P. Singh, Evaluation of fracture mechanics parameters in bimaterial systems using strain gages, Eng. Fract. Mech. 58 (1997) 273-283.

[15] P. Pranjol, K.S.R.K. Murthy, D. Chakraborty, A strain gage technique for mode I notch stress intensity factor of sharp V-notched configurations, Theor. Appl. Fract. Mech. 94 (2018) 57-70.

[16] P.R. Marur, H.V. Tippur, A strain gage method for determination of fracture parameters in bimaterial systems, Eng. Fract. Mech. 64 (1999) 87-104.

[17] R.J. Sanford, Principles of Fracture Mechanics, Prentice Hall, New York 2003.

[18] G.R. Irwin Analysis of stresses and strains near the end of a crack traversing a plate, J. Appl. Mech. 24 (1957) 361-364.

[19] P.R. Marur, R.C. Batra, G. Garcia, A.C. Loos, Static and dynamic fracture toughness of epoxy/alumina composite with submicron inclusions, J. Mater. Sci. 39 (2004) 1437-1440.

[20] L. Parnas, O.G. Bilir, Strain gage methods for measurement of opening stress intensity factor, Eng. Fract. Mech. 55 (1996) 485-492.

[21] S. Swamy, M.V. Srikanth, K.S.R.K. Murthy, P.S. Robi, Determination of complex stress intensity factors of complex configurations using strain gages, J. Mech. Mater. Struct. 3 (2008) 1239-1255.

[22] S. Rijal, H. Homma, Dimple fracture under short pulse loading, Int. J. Impact. Engng. 24 (2000) 69-83.

[23] J.F. Kalthoff, A. Burgel, Influence of loading rate on shear fracture toughness for failure mode transition, Int. J. Impact. Engng. 30 (2004) 957-971.

[24] M. Kirugulige, H.V. Tippur, Mixed-mode dynamic crack growth in a functionally graded particulate composite: experimental measurements and finite element simulations, J. Appl. Mech. 75 (2008) 051102-1-051102-14.

[25] M.J. Maleski, M.S. Kirugulige, H.V. Tippur, A method for measuring mode I crack tip constraint under static and dynamic loading conditions, Exp. Mech. 44 (2004) 522-532.

[26] S. Shirley, H. Homma, Approach to dynamic fracture toughness of GFRP from aspect of viscoelastic and debonding behaviors, J. Solid. Mech. Mater. Engng. 1 (2007) 275-286.

[27] H. Sarangi, K.S.R.K. Murthy, D. Chakraborty, Experimental verification of optimal strain gage locations for the accurate determination of mode I stress intensity factors, Eng. Fract. Mech. 110 (2013) 189-200.

[28] J.W. Dally, J.R. Berger, A strain gage method for determining K_I and K_{II} in a mixed mode stress field. The proceedings of the 1986 SEM spring conference on experimental mechanics, New Orleans, LA 1986 603-12.

[29] J.W. Dally, D.B. Barker, Dynamic measurements of initiation toughness at high loading rates, Exp. Mech. 8 (1988) 298-303.

[30] A. Shukla, B.D. Agarwal, B.Bhushan, Determination of stress intensity factor in orthotropic composite materials using strain gages, Eng. Fract. Mech. 32 (1989) 469-477.

[31] S.K. Khanna, A. Shukla, Development of stress field equations and determination of stress intensity factor during dynamic fracture of orthotropic composite materials, Eng. Fract. Mech. 47 (1994) 345-359.

[32] T. Kondo, M. Kobayashi, H.Sekine, Strain gage method for determining stress intensities of sharp-notched strips, Exp. Mech. 41 (2001) 1-7.

[33] A.Bürgel, H.S. Shin, D. Bergmanshoff, J.F. Kalthoff, Optimization of the strain-gauge-method for measuring mode-II stress intensity factors. In: The VIIth bilateral Czech/German symposium: significance of hybrid method for assessment of reliability and durability in engineering sciences, Liblice, Czech Republic str. 11, 1999.

[34] P. Pranjol, K.S.R.K. Murthy, D. Chakraborty, A strain gage technique for mode I notch stress intensity factor of sharp V-notched configurations, Theor. Appl. Fract. Mech. 94 (2018) 57-70.

[35] H. Sarangi, K.S.R.K. Murthy, D. Chakraborty, Optimum strain gage location for evaluating stress intensity factors in single and double ended cracked configurations, Eng. Fract. Mech. 77 (2010) 3190-3203.

[36] H. Sarangi, K.S.R.K. Murthy, D. Chakraborty, Radial locations of strain gages for accurate measurement of mode I stress intensity factor, Mater. Des. 31 (2010) 2840-2850.

[37] H. Sarangi, K.S.R.K. Murthy, D. Chakraborty, Extent of three parameter zone and optimum strain gage location for eccentric cracked configurations, Appl. Mech. Mat. 110-116 (2012) 127-134.

[38] H. Sarangi, K.S.R.K. Murthy, D. Chakraborty, Optimum strain gage locations for accurate determination of the mixed mode stress intensity factors, Eng. Fract. Mech. 88 (2012) 63-78.

[39] Debaleena Chakraborty, K.S.R.K. Murthy, D. Chakraborty, A new single strain gage technique for determination of mode I stress intensity factor in orthotropic composite materials, Eng. Fract. Mech. 124-125 (2014) 142-154.

[40] Debaleena Chakraborty, K.S.R.K. Murthy, D. Chakraborty, Determination of K_I in orthotropic laminates with double ended cracks using a single strain gage technique, Theor. Appl. Fract. Mech. 82 (2016) 96-106.

[41] Debaleena Chakraborty, D. Chakraborty, K.S.R.K. Murthy, A strain gage technique for the determination of mixed mode stress intensity factors of orthotropic materials, Compos. Struct. 160 (2017) 185-194.

[42] P. Pranjol, K.S.R.K. Murthy, D. Chakraborty, Effect of material properties on optimal radial strain gage locations in sharp V-notched configurations, MATEC Web of Conferences 172, 03002 (2018).

[43] H. Sarangi, K. Murthy, D. Chakraborty, Accurate Measurement of Mixed Mode (I/II) Stress Intensity Factors Using Strain Gages, J. Test. Eval. 45 (2017)751-762.

[44] Debaleena Chakraborty, K.S.R.K. Murthy, D. Chakraborty, Experimental determination of mode I stress intensity factor in orthotropic materials using a single strain gage, Eng. Fract. Mech. 173 (2017) 130-145.

[45] P.R. Marur, H.V. Tippur,Dynamic response of bimaterial and graded interface cracksunder impact loading, Int. J. Fract. 103 (2000) 95-109.

[46] R.J. Sanford, A critical re-examination of the Westergaard method for solving opening-mode crack problems, Mech. Res. Commun. 6 (1979) 289-294.

[47] J.W. Dally, W.F. Riley, Experimental stress analysis, Singapore, McGraw-Hill, 1991.